A Linear Doubly Salient Permanent-Magnet Motor With Modular and Complementary Structure

Ruiwu Cao[1,2], Ming Cheng[1], Chris Mi[2], Wei Hua[1], and Wenxiang Zhao[3]

[1]School of Electrical Engineering, Southeast University, Nanjing 210096, China
[2]College of Electrical and Computer Science, University of Michigan, Dearborn, MI 48185 USA
[3]School of Electrical and Information Engineering, Jiangsu University, Zhenjiang 212013, China

A linear doubly salient permanent magnet (LDSPM) motor is particularly suitable for long stator applications due to its simple and low cost stator, which consists of only iron. This paper proposes a new LDSPM motor design with complementary and modular structure. The key of this structure is that the primary mover is composed of two modules whose positions are mutually four and one half of the stator pole pitch apart and there is a flux barrier between them. Hence, the back electromotive force (EMF) waveform and cogging force of the two modules have 180 electrical degree differences. This design results in the total cogging force being significantly reduced and the back-EMF of each phase becoming symmetrical because the even harmonics are canceled. For fair comparison, an existing linear LDSPM motor is designed based on the same electromagnetic parameters and compared by the means of finite element analysis (FEA). The results reveal that the proposed LDSPM motor can offer symmetrical back-EMF waveforms, smaller cogging force, lower force ripple, and higher magnet utilization factor than the existing one.

***Index Terms*—Double salient motor, finite-element method, linear motor, permanent magnet (PM) motor.**

NOMENCLATURE

B_t	Magnet remanence.
e_k	Phase back-EMF.
F_e, F_{ek}	Three phase and one phase electromagnetic force.
F_r	Reluctance force.
F_{PM}	PM force.
F_N	Normal force.
F_{pm}	Magnetomotive force of PM excitation.
g	Air-gap length.
h_{st}	Stator tooth high.
h_{sy}	Stator yoke high.
h_{PM}	Permanent magnet high.
h_{mt}	Mover tooth high.
h_{my}	Mover yoke high.
i	Phase current.
k	Symbol of three phase, a, b, c.
l_m	Mover width.
L_{aa}	Self inductance of phase A.
M_{ab}	Mutual inductance between phase A and phase B.
x	Mover position.
P	Out put power.
R_{pm}	Reluctance of the PM.
R_σ	Leakage reluctance.
$R_a \sim R_c$	Phase reluctance.
R_δ	Air-gap reluctance.
R_{sy}	Stator yoke reluctance.
R_k	Phase resistance.
μ_r	Magnet relative recoil permeability.
μ_0	Magnet permeability of free space.
V_{mag}	Total magnet volume.
v	Mover mechanical speed.
w_{st}	Stator tooth width.
w_{ss}	Stator slot width.
w_{PM}	Permanent magnet width.
w_{mt}	Mover tooth width.
w_{st}	Mover slot width.
w_{ay}	Mover plus yoke width.
$w_a \sim w_c$	Overlapping width between stator and mover teeth.
w_δ	Sum of $w_a \sim w_c$.
τ_m	Mover pole pitch.
τ_s	Stator pole pitch.
Φ_{pm}	PM flux.
Φ_δ	Air gap flux equal to the sum of three phase fluxes.
$\Lambda_a \sim \Lambda_c$	Phase permeance.

Manuscript received February 28, 2011; revised May 10, 2011; accepted June 13, 2011. Date of publication June 23, 2011; date of current version November 23, 2011. Corresponding author: M. Cheng (e-mail: mcheng@seu.edu.cn).

Color versions of one or more of the figures in this paper are available online at http://ieeexplore.ieee.org.

Digital Object Identifier 10.1109/TMAG.2011.2160554

0018-9464/$26.00 © 2011 IEEE

Λ_δ	Sum of the three phase permeance.
ψ_{pm}	PM flux linkage.
ψ_{aa}	Flux linkage of phase A by the PMs and i_a.
ψ_{ab}	Flux linkage in phase A by the magnet i_b.
ψ_k	Phase flux linkage.

I. Introduction

At present, a new class of stator permanent magnet (PM) brushless motor, namely the doubly salient PM (DSPM) motor [1], flux-reversal PM (FRPM) machine, [2] and flux-switching PM machine [3] has received wide attention [4]–[9]. The stator-PM motor incorporates the merits of both a switched reluctance motor (SRM) and a PM brushless motor, in which both the PM and the armature windings are on the stator while the rotor is the same as a SRM. Hence, it offers the advantage of excellent mechanical integrity, high power density, fault tolerance, and is free from irreversible demagnetization of the magnets. It should be noted that the operation principle and electromagnetic performance of the three machines are different [10]. The linear DSPM motor [11], [12], linear FRPM motor [13], [14], and linear FSPM motor [15]–[18], named as primary-PM linear motors, also have been investigated, in which both the PMs and armature windings of those motor are set on the short mover while the long stator is only made of iron. Obviously, the primary-PM linear motors incorporate the merits of both stator-PM motor and permanent magnet linear synchronous motor (PMLSM) [19]–[22]. Hence, it is perfectly suitable for long stator applications, such as urban rail transit, resulting in considerable reduction of system cost due to its simple and cheap stator.

In this paper, a new design of the linear DSPM motor will be investigated. Fig. 1 shows a 12/8-pole rotary DSPM motor, and its operation principle and fault-tolerance operation are discussed in [23]. Very recently, a linear DSPM motor (Motor_1) as shown in Fig. 2(a), has been investigated [11], which can be obtained by splitting the 12/8-pole rotary DSPM motor as shown in Fig. 1 along the radial direction and unrolling it. Then, in order to balance the magnet circuit of the end coils, two additional teeth and one half piece of PM are added at each end of the primary mover. The results listed in [11] show that two additional teeth at each end of Motor_1 are enough to balance the magnet circuits of the coils located at the end of the primary mover. However, this motor also suffers from drawbacks such as asymmetrical back-electromotive force (EMF) and large cogging force as in a rotary DSPM motor with unskewed rotor [24]. In [25], a new method by shifting the additional teeth position to mitigate the force ripple in linear FSPM motor is proposed. However, the effect isn't obvious for Motor_1, hence this method was not adopted in this paper. Also, the additional teeth increase the mover length and weight.

In this paper, in order to solve the problems in Motor_1, namely asymmetrical back-EMF and high cogging force, a LDSPM motor (Motor_2) with modular and complementary structure is proposed and investigated. The finite-element method (FEM) is used to validate the concepts. For comparison, both motors are designed with the same electromagnetic parameters.

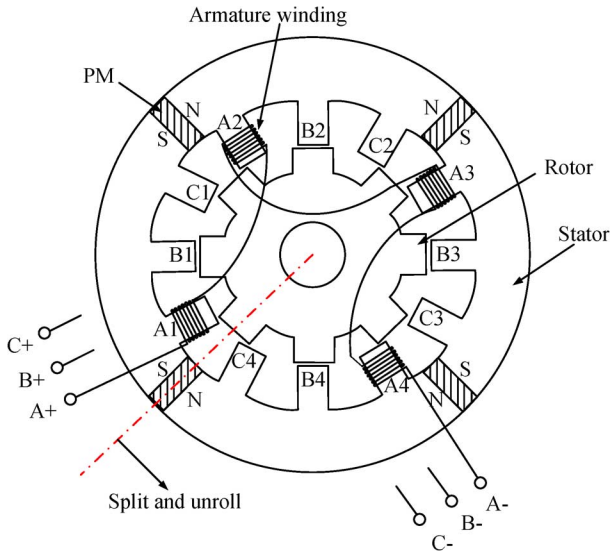

Fig. 1. Cross section of the 12/8 DSPM motor.

II. Topology and Operation Principle

A. Topology and Operation Principle

The topology of Motor_2 is shown in Fig. 2(b). Different from Motor_1, its mover consists of two modules whose positions are mutually four and one half of the stator pole pitch (namely 180° electrical degree) apart and there is a flux barrier between the two adjacent modules. In addition, only one PM is inserted in the mover iron of each mover part. The two magnets are magnetized in alternate directions. Similar to a linear switched reluctance motor (LSRM) [26] and Motor_1, concentrated armature windings are adopted, which are wound around the mover teeth of each mover part. Also, each phase winding is composed of four concentrated coils connected in series, e.g., coil A1 $\sim$ coil A4 for phase A, same as that of Motor_1. However, since two mover parts have 180° electrical degree shift, therefore the variation trend of electromagnetic parameters versus mover position in coil (A1+A2) and coil (A3+A4) of both motors are different. Assuming that the PM flux linkage of coil (A1+A2) reaches the negative maximum value at the position shown in Fig. 2(b), then the PM flux linkage of coil (A3+A4) reaches the positive minimum value. Consequently, as the mover moves to the right, the PM flux linkage waveform versus mover position in coil (A1+A2), coil (A3+A4), phase A and the phase back-EMF waveform of Motor_2 are shown in Fig. 3(a). It should be noted that the flux linkages induced in coil (A1+A2) and coil (A3+A4) are unipolar, while the flux linkage of phase A is bipolar. In contrast, the flux linkages induced in coil (A1+A2), coil (A3+A4) and phase A of Motor_1 are all unipolar as shown in Fig. 3(b).

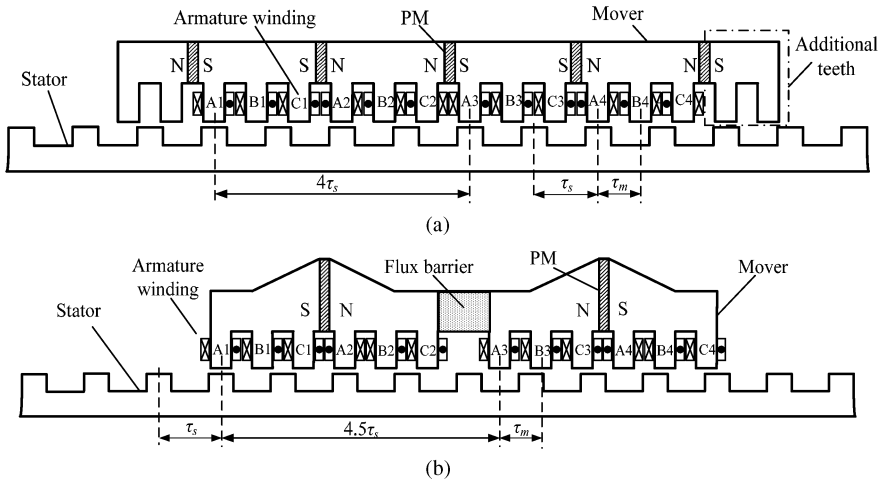

Fig. 2. Cross-section of linear DSPM motors. (a) Motor_1. (b) Motor_2.

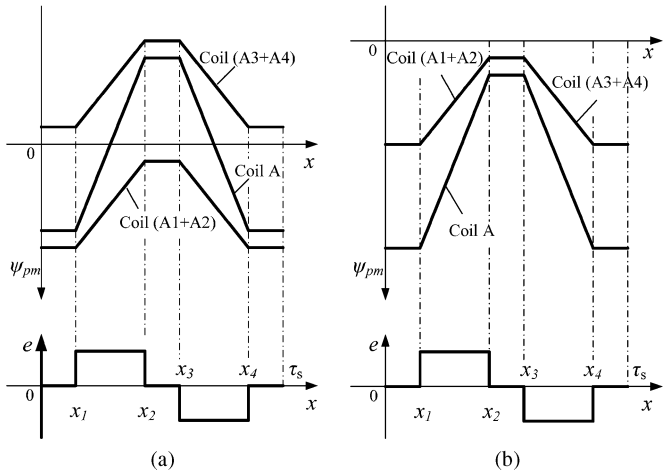

Fig. 3. The operation principle of both LDSPM motors. (a) Flux linkage and back-EMF of Motor_2. (b) Flux linkage and back-EMF of Motor_1.

B. Geometry Design

Because Motor_1 is the linear structure of a 3-phase 12/8-pole DSPM motor, we can design this motor by using the methods discussed in [27], [28].

The mover and stator teeth width should comply with the conditions below.

First, to minimize the permeance when the mover teeth are at unaligned position, the mover and stator teeth width should satisfy the relationship

$$w_{mt} + w_{st} < \tau_s \tag{1}$$

where w_{mt} is mover teeth width, w_{st} is stator teeth width, and $\tau_{\rm s}$ is stator pole pitch.

Second, according to the operation principle of DSPM motor, to ensure successful current reversal, the mover teeth and stator teeth width should be

$$w_{st} > w_{mt}. \tag{2}$$

By arranging two additional teeth at each end of primary mover, the magnetic circuit of the end coil can be balanced [11]. So, the no-load magnetic circuit of Motor_1 can be simplified as shown in Fig. 4(a), where F_{pm} is the magnetomotive force of PM excitation, R_{pm} is the reluctance of the PM pole, R_σ is the leakage reluctance, Φ_{pm} is the PM flux, Φ_δ is the air gap flux equal to the sum of three phase fluxes, and $R_a \sim R_c$ are the phase reluctance of each phase. To simplify the analysis, the mover iron core is assumed to be of infinite permeability, and the stator yoke reluctance is denoted as $R_{\rm sy}$. The permeance of one phase Λ_a and the sum of the three phase Λ_δ can be expressed as

$$\Lambda_a = \frac{1}{R_a} = \mu_0 \frac{w_a l_m}{2g} \tag{3}$$

$$\Lambda_\delta = \frac{1}{R_\delta} = \mu_0 \frac{w_\delta l_m}{2g} \tag{4}$$

where w_a is the overlapping length of phase A mover teeth with stator teeth, w_δ is the overlapping length of three phases mover teeth with stator teeth, g is the air-gap length.

Third, similar to the rotary DSPM motor, it can also be proved that when mover teeth width w_{mt} is chosen by

$$w_{mt} = \frac{1}{2}\tau_m. \tag{5}$$

The sum of overlapping length w_δ is kept constant:

$$w_\delta = w_a + w_b + w_c = w_{st} \tag{6}$$

where τ_m is mover pole pitch. In this paper $\tau_m/\tau_s = 8/12$, $w_a \sim w_c$ is overlapping length between the mover teeth of phase A, phase B, phase C, and the stator teeth, respectively.

Hence, the total permeance of three phases Λ_δ is nearly constant when motor is in operation, while each phase permeance $\Lambda_a \sim \Lambda_c$ is variable. So the operation point of PMs does not change with the mover position.

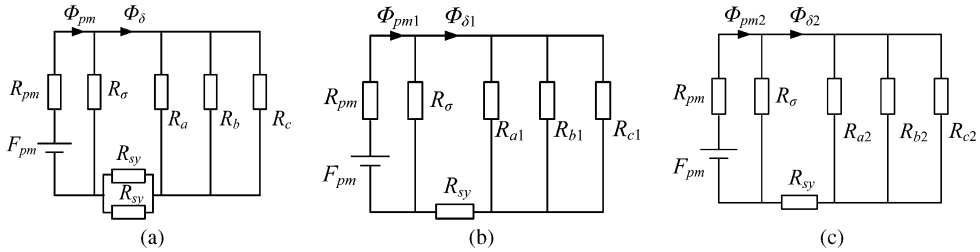

Fig. 4. Simplified equivalent magnetic circuit of both motors. (a) Motor_1. (b) Left model of Motor_2. (c) Right model of Motor_2.

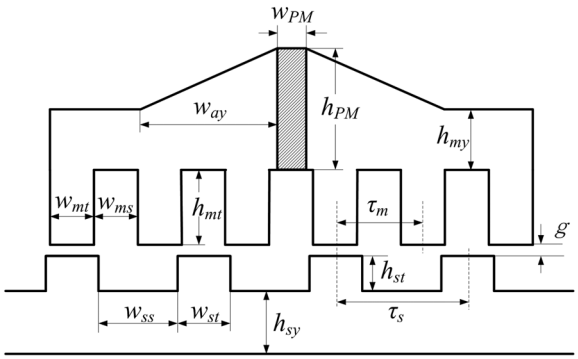

Fig. 5. Determination of motor dimensions.

Also, the stator teeth width w_{st} is chosen:

$$w_{st} - w_{mt} = 2x_1 = \frac{1}{3}w_{mt} \tag{7}$$

where x_1 is the mover distance as shown in Fig. 3.

For fair comparison, Motor_2 is designed with the same dimensions as Motor_1, including, τ_m, τ_s, w_{mt}, the mover teeth height $h_{\rm mt}$, the stator teeth dimensions, air-gap length g, the number of turns per coil N_{coil} and the slot fill factor. However, the phase armature windings of Motor_1 are excited by two parallel magnets, while Motor_2 is only excited by one magnet. Hence, in order to get the same electromagnetic parameters, the height of the magnet in Motor_2 is twice of that of Motor_1 and the width of the magnet is the same as Motor_1.

The no-load magnetic circuit of Motor_2 can be simplified as shown in Fig. 4(b) and (c).

The permeance of one phase Λ_{a1} and the sum of the three phase $\Lambda_{\delta 1}$ in the left model can be expressed as

$$\Lambda_{a1} = \frac{1}{R_{a1}} = \mu_0 \frac{w_{a1} l_m}{2g} \tag{8}$$

$$\Lambda_{\delta 1} = \frac{1}{R_{\delta 1}} = \mu_0 \frac{w_{\delta 1} l_m}{2g} \tag{9}$$

where w_{a1} is the overlapping length between phase A mover teeth in the left model and stator teeth. Obviously, Λ_{a1} and $\Lambda_{\delta 1}$ has the same performance with that of Motor_1, namely, $\Lambda_{\delta 1}$ keeps constant and Λ_{a1} changes with the mover position.

The total permeance of phase A of Motor_2 can be expressed as

$$\Lambda_a = \Lambda_{a1} + \Lambda_{a2} = \mu_0 \frac{(w_{a1} + w_{a2}) l_m}{2g} \tag{10}$$

where Λ_{a2} is the permeance of phase A in the right model, w_{a2} is the overlapping length between phase A mover teeth in the right model and stator teeth.

As can be seen from (10) and Fig. 2(b), the range of variation of $w_{a1} + w_{a2}$ with mover position is very small. In fact, if the stator teeth width is chosen by

$$w_{st} = \frac{1}{2}\tau_s \tag{11}$$

the total overlapping length between phase A mover teeth and stator teeth $w_{a1} + w_{a2}$ is kept constant:

$$w_{a1} + w_{a2} = w_{mt}. \tag{12}$$

Then the three phase permeance $\Lambda_a, \Lambda_b, \Lambda_c$, and the sum of three phase Λ_δ in Motor_2 are all nearly constant when the motor is in operation. So, the variation of phase inductance without considering the magnetic saturation versus mover position will be small.

As can be seen from Fig. 4, the stator yoke reluctance of Motor_2 is twice of that in Motor_1. Hence, the flux density in the stator yoke of Motor_2 will be higher than that of Motor_1 when the two motor has the same stator dimension.

The key dimensions are defined in Fig. 5 and listed in Table I. It can be seen that the mover weight of Motor_2 is 17.2 kg, which is only 89% of that of Motor_1. Also, the total volume of PMs in motor_2 is only 80% of that of Motor_1. However, because the mover of Motor_2 is higher than Motor_1, it is necessary to adopt some approaches to optimize the PM shape and fixture to reduce the mover height. But in this paper, this dimension is used directly to compare the electromagnetic performance of Motor_2 and Motor_1.

III. Comparison of Performance of the Two Motors

Maxwell 2D has been used to analyze the performance of the rotary DSPM motor [29], [30] and the permanent-magnet linear motor [31], [32]. Hence, the transient solver of this software is used to study the electromagnetic characteristics of the two LDSPM motors discussed in this paper.

TABLE I
DESIGN SPECIFICATIONS OF BOTH MOTORS

Items	Motor_1	Motor_2
Rated speed, v (m/s)	3	
Mover width, l_m (mm)	120	
Mover tooth width, w_{mt} (mm)	16.5	
Mover slot width, w_{ms} (mm)	16.5	
Mover tooth high, h_{mt} (mm)	19	
Mover yoke high, h_{my} (mm)	26	
Mover add yoke width, w_{ay} (mm)	54.75	
Mover pole pitch, τ_m (mm)	33	
Stator pole pitch, τ_s (mm)	49.5	
Stator tooth width, w_{st} (mm)	22	
Stator slot width, w_{ss} (mm)	27.5	
Stator tooth high, h_{st} (mm)	15	
Stator yoke high, h_{sy} (mm)	22	
Iron material	D23	
Permanent magnet high, h_{PM} (mm)	26	52
Permanent magnet width, w_{PM} (mm)	6	
Total magnet volume, V_{mag} (mm^3)	5*26*120*6	2*52*120*6
Magnet remanence, B_t (T)	1.2	
Magnet relative recoil permeability, μ_r	1.05	
Air gap length, g (mm)	0.8	
Number of turns per coil, N_{coil}	74	
Rate current, I_{RMS} (A)	6	
Mover iron volume, V_{iron} (cm^3)	2104.2	1850.76
Mover weight, m_{mover} (kg)	19.32	17.2

A. Open Circuit Field Distributions

Fig. 6(a) and (b) shows the open circuit flux distributions of the two motors at the initial position. It can be seen that the flux linkage excited in phase A of both motors reaches the negative maximum value. However, the magnetic circuits of both motors are different. In the case of Motor_1, the main flux path of coil A2 can be expressed as: PM_N—mover teeth A2—air-gap—stator teeth and yoke—air-gap—mover teeth B and C—PM_S. The main flux path for coil A1, coil A2, and coil A4 is the same as that of coil A2. For Motor_2, the main flux path of coil A2 in the left mover part can be expressed as: PM_N—mover teeth A2—air-gap—stator teeth and yoke—air-gap—mover teeth A1, B1, and C1—PM_S, which is the same with that of coil A1, while in the right part of the flux linkage excited in coil A1 and coil A2 are very little. The flux density in both motors is shown in Fig. 6(c) and (d). It should be noted that the flux density in stator yoke is about twice as high for Motor_2 versus Motor_1, which will increase the stator mass, cost, and weight.

Fig. 7 shows the corresponding air-gap magnetic flux density of both motors in the range of 11 times τ_s distances as shown in Fig. 6. It is found that the amplitude and shape of air-gap flux density of both motors are the same in the displacement range from τ_s to $5\tau_s$. This illustrates that the magnetic loading of both motors are the same. For Motor_1 as shown in Fig. 7(a), the air-gap flux density distribution (displacement range from $5\tau_s$ to $9\tau_s$) is nearly the same as that of the left part. For motor_2, because the right part of Motor_2 has 180° electrical degree shift from the left part, the air-gap flux density distribution of the right part (displacement range from $6\tau_s$ to $10\tau_s$) is different from that of the left part. It should be noted that the additional teeth can balance the magnetic circuit of coils at each end part of Motor_1.

Fig. 8 shows the air-gap magnetic flux density of both motors by the PMs and positive armature current i_b. For Motor_1 as shown in Fig. 8(a), the air-gap flux density under the conducting mover pole is increased whereas that under the nonconducting pole is decreased and vice versa. However, the total effective flux of the three phases does not significantly change, indicating that the air-gap flux in Motor_1 is mainly contributed by PMs. For Motor_2 as shown in Fig. 8(b), the air-gap magnetic flux density of the left mover is the same as that of Motor_1. For the right mover of Motor_2, the air-gap flux density under the conducting mover pole is decreased whereas that under the non-conducting pole is increased and vice versa. The total effective flux of the three phases also does not significantly change. This illustrates that the effect of armature reaction flux to the PM flux is insignificant. The reason is that most of the armature reaction flux loops through adjacent mover poles and very little through the PMs.

B. Flux Linkage and Back-EMF

The flux linkage versus mover position of Motor_2 can be obtained by Maxwell 2D FEA as shown in Fig. 9(a). It can be seen from Fig. 9(a) that the simulation results agree with the

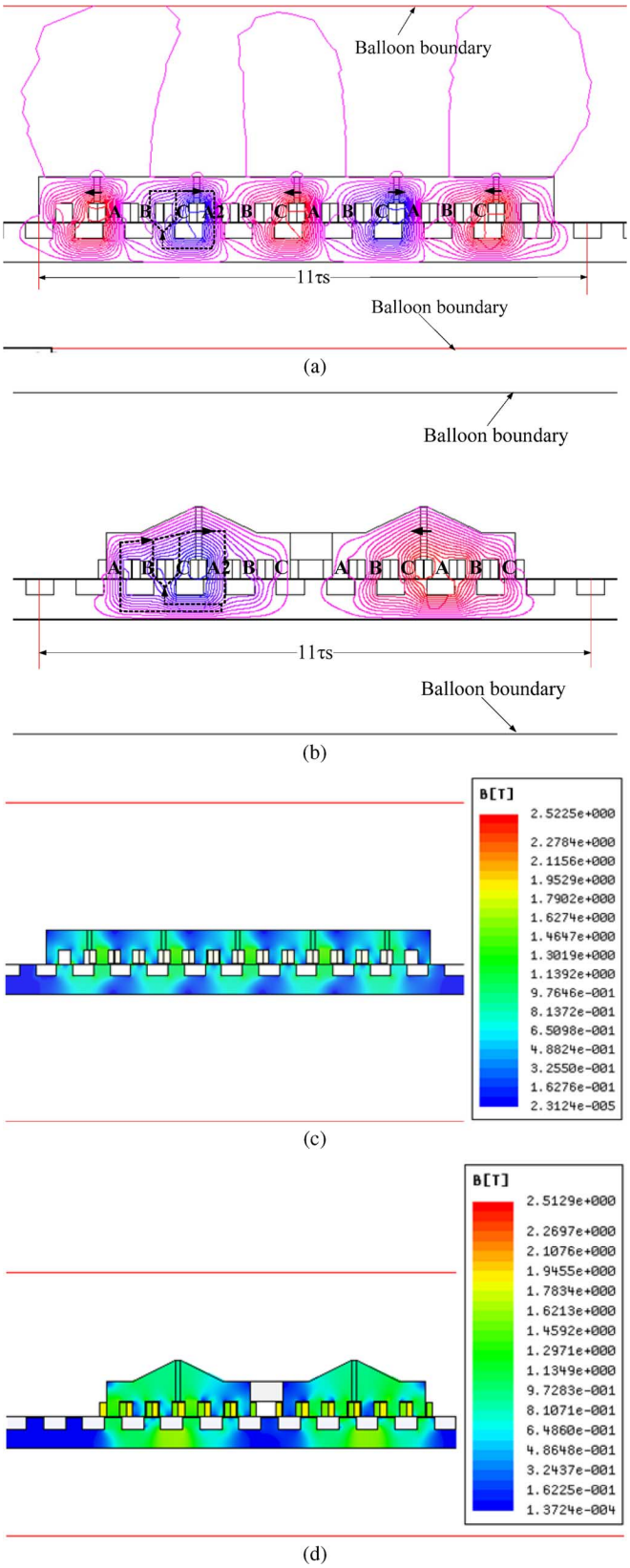

Fig. 6. Open circuit field and flux density distributions of both motors. (a) Field distribution in Motor_1. (b) Field distribution in Motor_2. (c) Flux density of Motor_1. (d) Flux density of Motor-2.

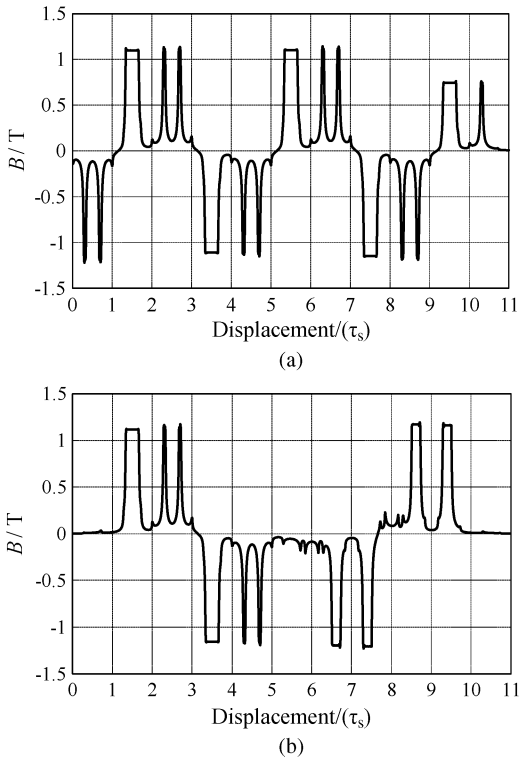

Fig. 7. Open load air-gap flux density distributions at initial position. (a) Motor_1. (b) Motor_2.

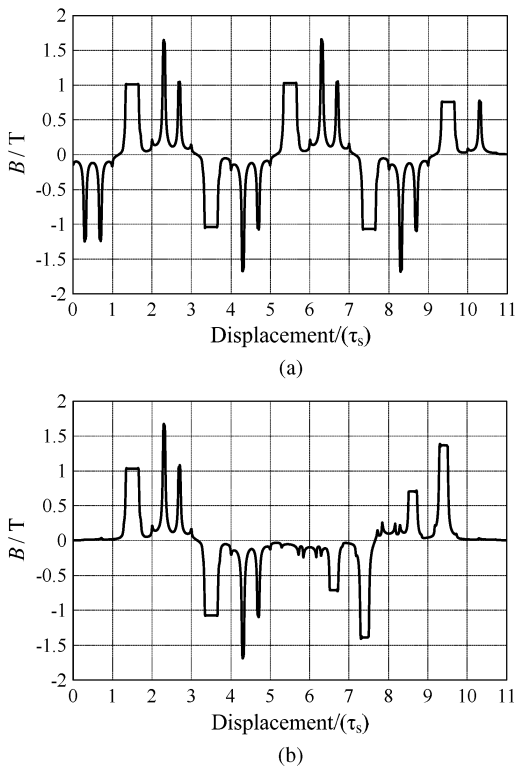

Fig. 8. Air-gap flux density distributions at load condition (PMs and $i_b = 6$ A). (a) Motor_1. (b) Motor_2.

theoretic analysis as shown in Fig. 3(a). Meanwhile, the corresponding back-EMF waveforms induced in coil (A1+A2), coil (A3+A4), and phase A at the rated speed are shown in Fig. 9(b). It can be seen that the back-EMF waveforms induced in coil (A1+A2) and coil (A3+A4) are asymmetrical and slant to the

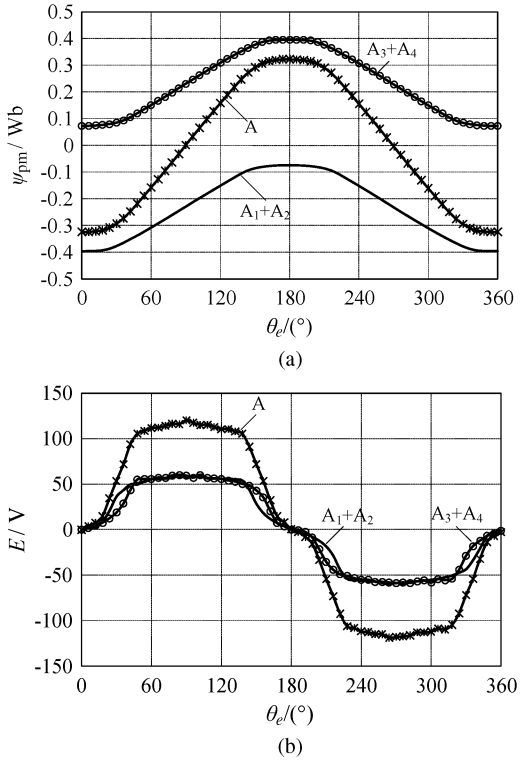

Fig. 9. PM flux linkage and EMF versus mover position of Motor_2. (a) PM flux linkage. (b) EMF.

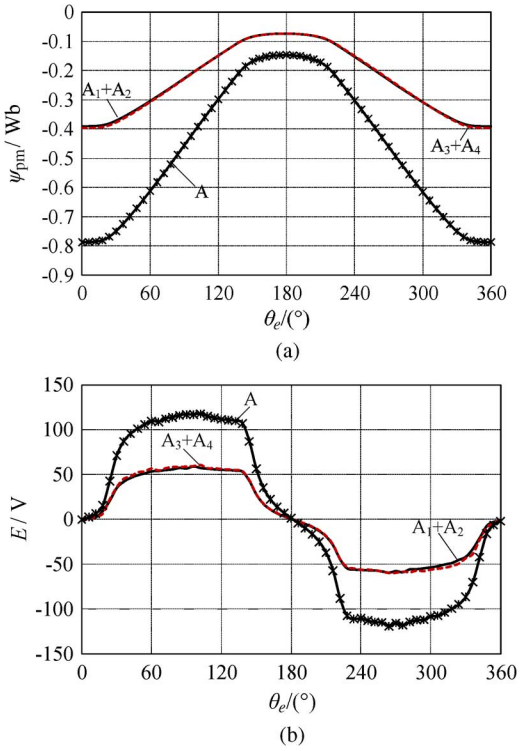

Fig. 10. PM flux linkage and EMF versus mover position of Motor_1. (a) PM flux linkage. (b) EMF.

right and left, respectively, but the phase are the same. However, the back-EMF induced in phase A is symmetrical and its amplitude is twice that of coil (A1+A2) and coil (A3+A4).

On the other hand, for Motor_1, the flux linkage and back-EMF waveforms induced in coil (A1+A2), coil (A3+A4), and coils of phase A are shown in Fig. 10(a) and Fig. 10(b), respectively. Obviously, the back-EMF waveforms are all asymmetrical.

Fig. 11(a) shows the three phase PM flux linkage waveforms and the detailed values, namely, maximum value ψ_{pm_max}, minimum value ψ_{pm_max}, peak-peak value ψ_{pm_pp} are listed in Table II. It should be noted that the peak to peak PM flux linkage in phase B of both motors is bigger than that in phases A and C. The reason is that phases A and C have teeth on the extremes of the mover, whereas phase B is located in the middle.

The three phase back-EMF waveforms of both motors versus mover position are shown in Fig. 11(b). In order to compare the back-EMF of both motors, the harmonics of the back-EMF waveforms have been analyzed. Fig. 12 shows the harmonic contents of the back-EMF of each motor using discrete Fourier transform. It can be seen that the even harmonics in the back-EMF of Motor_2 are significantly reduced and the third, fifth, and seventh harmonics in the back-EMF of both motors are significant.

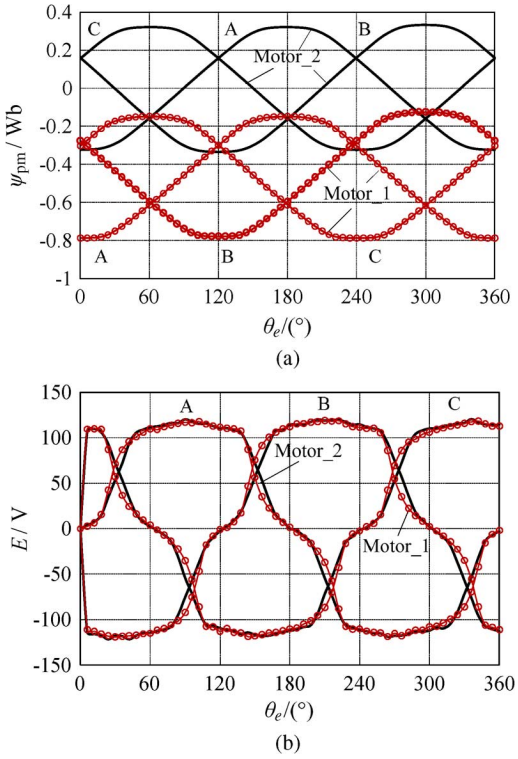

Fig. 11. Flux linkage and back-EMF versus mover position of both motors. (a) Flux linkage; (b) back-EMF.

C. Self and Mutual Inductance

In order to calculate the inductance accurately, the method considering the magnetic saturation is adopted to analyze the inductance of flux switching permanent magnet (FSPM) motor and DSPM motor [33], [34]. In this paper, this method is also

TABLE II
PM FLUX LINKAGE OF BOTH MOTORS

	Motor_1 (Wb)			Motor_2 (Wb)		
Phase	A	B	C	A	B	C
ψ_{pm_max}	0.323	0.333	0.324	-0.147	-0.123	-0.146
ψ_{pm_min}	-0.324	0.333	-0.323	-0.788	-0.778	-0.787
ψ_{pm_pp}	0.647	0.666	0.647	0.641	0.655	0.641

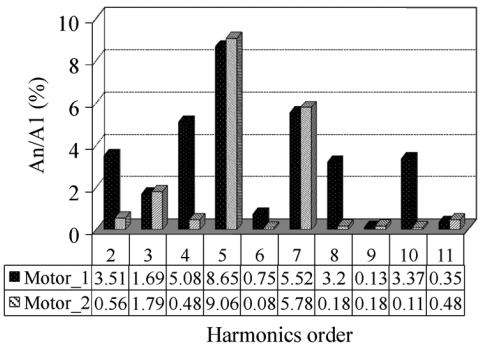

Fig. 12. Harmonic analysis of back-EMF.

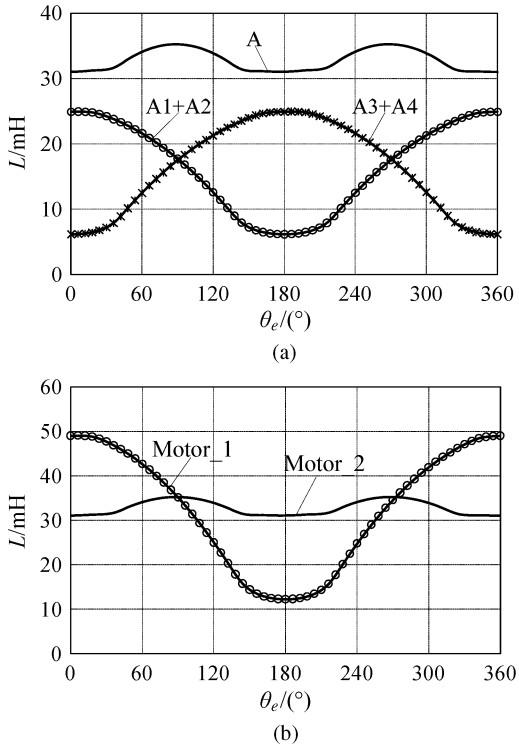

Fig. 13. The self inductance without considering magnetic saturation. (a) Coils and self-inductance of motor_2. (b) Comparison of self inductance of both motors.

used to compute the self inductance and mutual inductance of the two LDSPM. The inductance can be expressed as

$$L_{aa} = (\psi_{aa} - \psi_{pm})/i \tag{13}$$

$$M_{ab} = (\psi_{ab} - \psi_{pm})/i \tag{14}$$

where ψ_{aa} is the total excitation flux linkage in coils of phase A produced by the magnet and phase A current, ψ_{ab} is the total excitation flux linkage in coils of phase A produced by the magnet and phase B current, ψ_{pm} is the magnet flux linkage at no-load, L_{aa} is the self inductance of phase A, M_{ab} is the mutual inductance between phase A and phase B, i is the applied phase current.

Fig. 13(a) shows the self inductance in coil (A1+A2), coil (A3+A4) and phase A of Motor_2 without considering magnetic saturation. A current $i = +6$ A is applied to the phase winding while the magnets are set as air material. It can be seen that the self inductance in coil (A1+A2) and coil (A3+A4) are almost the same but with 180° electrical degree shift. Hence, when they connect in series the variation of phase A self inductance versus mover position is small. This result is the same as that discussed in part II by means of magnetic circuit analysis. Then, the phase A self inductance of both motors are compared in Fig. 13(b).

Fig. 14 shows the self inductance characteristics of both motors, where "+6 A", "PM+6 A" and "PM-6 A" denotes three different excited methods, namely without considering magnetic saturation, strengthening and weakening action of the armature flux (applied +6 A and −6 A phase current to the mover winding), respectively. For Motor_1, as shown in Fig. 14(a), the inductance under "PM+6 A" is lower than that under "PM-6 A", especially in the range from 0° to 140° and 220° to 360° electrical degree due to the higher saturation under "PM+6 A".

For Motor_2, as shown in Fig. 14(b), it illustrates that the inductance under "PM+6 A" is lower than that under "PM-6 A" especially in the range from 0° to 90° and 270° to 360°electrical degree due to magnetic saturation. In addiction, the self inductance under "PM+6 A" and "PM-6 A" are almost the same but with 180° electrical degree shift. Moreover, the mutual inductance of both motors under different loads is depicted in Fig. 15. It can be observed from Fig. 15 that the mutual inductance variation of Motor_1 is bigger than that of Motor_2.

D. Cogging Force

In order to better understand the cogging force of Motor_2, the cogging force analysis is carried out in three steps. First, the mover only consists of the left mover part, thus the cogging force is computed and denoted as "Left" shown in Fig. 16(a). Second, the mover only consists of the right part, thus the cogging force is computed and denoted as "Right" as shown in Fig. 16(a). It should be noted that the "Left+Right" as shown in Fig. 16(a) denotes the total cogging force waveform of the previous two steps. Third, the cogging force of the entire mover consisting of the left and the right part is computed and denoted as "whole", which is compared with the "Left+Right" cogging force as shown in Fig. 16(b). It is clear that the total cogging

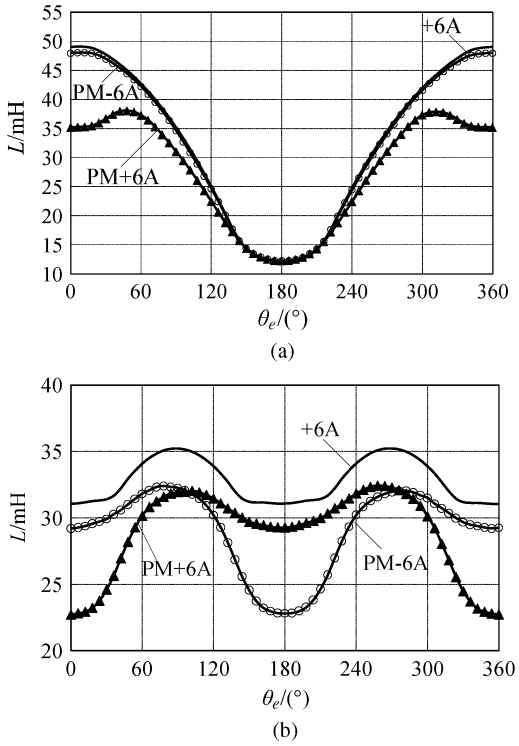

Fig. 14. The self inductance of both motors at different loads. (a) Motor_1. (b) Motor_2.

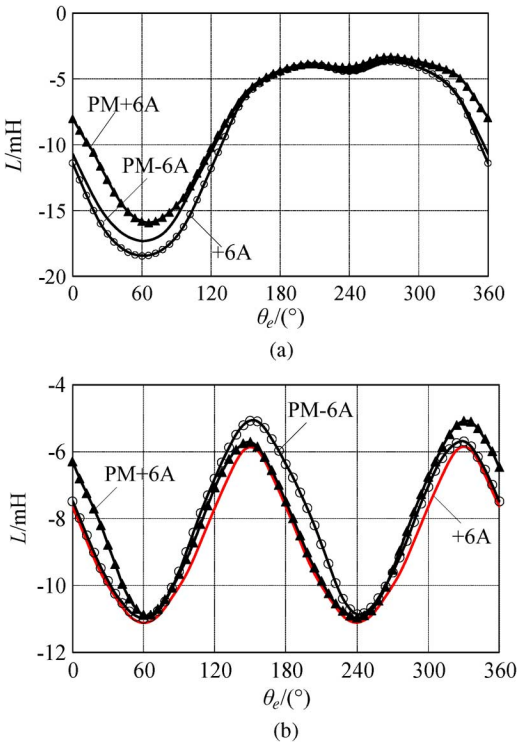

Fig. 15. The mutual inductance of both motors at different loads. (a) Motor_1. (b) Motor_2.

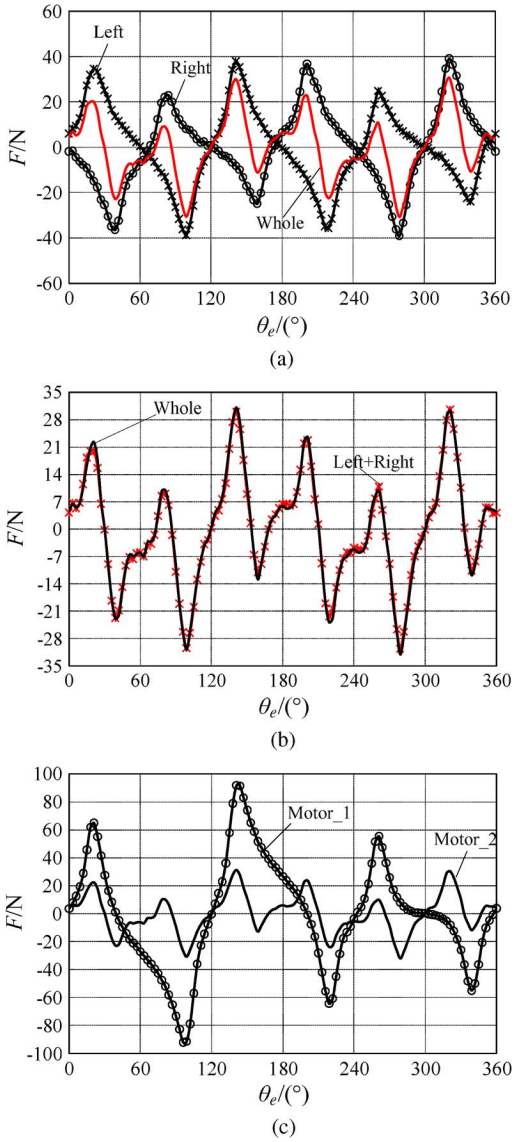

Fig. 16. Cogging force analysis. (a) Partial and sum cogging force of Motor_2. (b) Cogging force of Motor_2 based on two methods. (c) Cogging force of both motors.

force of Motor_2 is nearly the same as the total cogging force of left and right parts. Due to the 180° electrical degrees shift of cogging force of the two parts in Motor_2, the total cogging force of Motor_2 is significantly reduced.

Fig. 16(c) compares the cogging force of both motors. For Motor_1, the peak to peak cogging force is 183.7 N, while for Motor_2 the cogging force ripple has been reduced to 63.2 N. So the force ripple is reduced by 65.6%.

E. Thrust Force

For the proposed LDSPM motor, the voltage equation for each mover armature winding is expressed as

$$u_k = R_k i_k + e_k = R_k i_k + d\psi_k/dt \tag{15}$$

where, $k = a, b, c$ denotes each of the three phases. R_k is the phase resistance. The flux linkage ψ_k consists of the magnet in-

duced flux linkage ψ_{pmk} and the armature reaction flux linkage $(L_k i_k)$

$$\psi_k = L_k i_k + \psi_{pmk} \tag{16}$$

Therefore, the phase back-EMF is expressed as

$$e_k = \frac{d\psi_k}{dt} = L_k \frac{di_k}{dt} + i_k \frac{dL_k}{dt} + \frac{d\psi_{pmk}}{dt} \tag{17}$$

Hence, each phase input power is given below, neglecting the iron loss

$$\begin{aligned} p_k &= i_k L_k \frac{di_k}{dt} + i_k^2 \frac{dL_k}{dt} + i_k \frac{d\psi_{pmk}}{dt} \\ &= \frac{d}{dt}\left(\frac{1}{2} i_k^2 L_k\right) + \left(\frac{1}{2} i_k^2 \frac{dL_k}{dx} + i_k \frac{d\psi_{pmk}}{dx}\right) v \end{aligned} \tag{18}$$

where $v = d_x/d_t$ is the mover speed, $i_k^2 L_k/2$ is armature reaction field energy.

Since $P = Fv$, thus, the second term of (18) represents the electromagnetic force of phase k,

$$F_{ek} = \frac{1}{2} i_k^2 \frac{dL_k}{dx} + i_k \frac{d\psi_{pmk}}{dx} \tag{19}$$

The three phase electromagnetic force can be expressed as

$$\begin{aligned} F_e &= \sum_{k=a}^{c} F_{ek} \\ &= \sum_{k=a}^{c} \left[\frac{1}{2} i_k^2 \frac{dL_k}{dx} + i_k \frac{d\psi_{pmk}}{dx}\right] \\ &= \sum_{k=a}^{c} \left(\frac{1}{2} i_k^2 \frac{dL_k}{dx}\right) + \sum_{k=a}^{c} \left(i_k \frac{d\psi_{pmk}}{dx}\right) \\ &= F_r + F_{PM} \end{aligned} \tag{20}$$

where, $F_r = \sum_{k=a}^{c}((1/2) i_k^2 (dL_k/dx))$ is the reluctance force, and $F_{PM} = \sum_{k=a}^{c}(i_k (d\psi_{pmk}/dx))$ is the force produced by the magnets.

Traditionally, the rotary DSPM motor adopts the brushless DC (BLDC) operation and operates at brushless AC (BLAC) mode when its back-EMF is sinusoidal with skewed rotor. Recently, a trapezoidal back-EMF PM and a DSPM motor operating at BLAC mode without considering the reluctance torque has been discussed in [23] and [35]. In this paper, the electromagnetic force characteristics considering the reluctance force of two LDSPM motors operating at BLDC and BLAC modes as shown in Fig. 17 will be discussed.

Fig. 17(a) depicts the conventional BLDC operation with 120° conduction. In this operation, E_m is the top flat value of EMF. The applied DC current yields

$$I_m = k_{i\_BLDC} I_{rms\_BLDC} = \sqrt{\frac{3}{2}} I_{rms\_BLDC} = 6\sqrt{\frac{3}{2}}\ (\mathrm{A}) \tag{21}$$

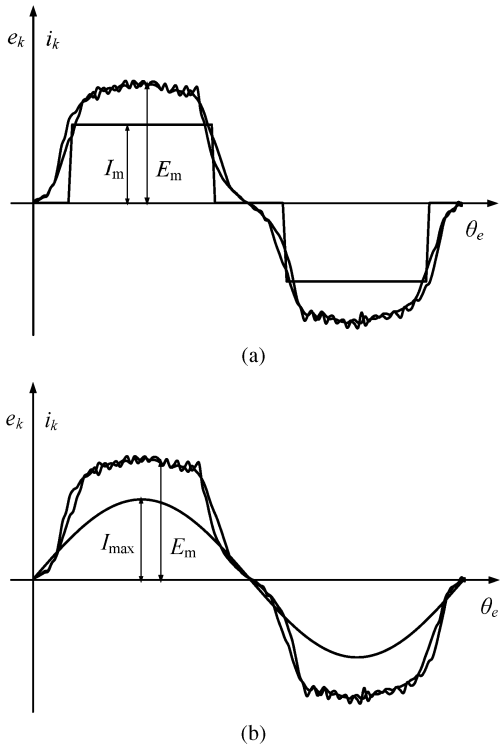

Fig. 17. BLDC and BLAC operation model under trapezoidal back-EMF. (a) BLDC operation model. (b) BLAC operation model.

where, $I_{rms\_BLDC} = 6$ A is the RMS current.

Fig. 17(b) depicts the BLAC operation under trapezoidal back-EMF of LDSPM. In this operation, $i_d = 0$ control method is adopted, namely keeping the applied current in phase with the back-EMF. Also, the applied RMS current is equal to that applied in BLDC operation. Thus, the peak current satisfies:

$$I_{\max} = k_{i\_BLAC} I_{rms\_BLAC} = \sqrt{2} I_{rms\_BLDC} = 6\sqrt{2}\ (\mathrm{A}) \tag{22}$$

Hence, the reluctance thrust force waveforms of both motors under BLDC and BLAC operation can be obtained and shown in Fig. 18 by using (20), (21), (22), and the self inductance shown in Fig. 14. For the BLDC operation shown in Fig. 18(a), it is found that the reluctance force ripple (68.7 N) of Motor_2 is about 87.5% of that of Motor_1. On the other hand, for the BLAC operation, the reluctance force ripple (28.9 N) of Motor_2 is only about 23% of Motor_1. The results show that Motor_2 is more suitable for BLAC operation than Motor_1.

Fig. 19 shows the electromagnetic thrust force F_e of both motors under BLDC and BLAC operation calculated using FEM. The corresponding force parameters are listed in Table III, where F_{e_max}, F_{e_min}, F_{e_avg} and F_{e_rip} are the maximum, minimum, average and ripple thrust force, respectively. It can be observed that F_{e_avg} of Motor_2 under BLDC operation is a little bigger than that of Motor_1, while F_{e_rip} of Motor_2 is only about 82.8% of Motor_1. On the other hand, for the BLAC operation, Motor_2 can also offer a little bigger average thrust force F_{e_avg} than Motor_1 and reduce F_{e_rip} to only 21.6% of that of Motor_1. The results illustrate that the Motor_2 can

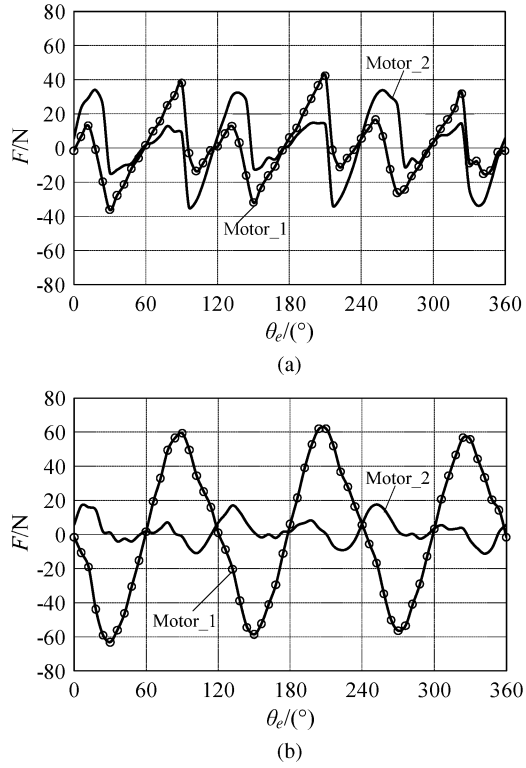

Fig. 18. The reluctance thrust force of both motors under BLDC and BLAC operation modes. (a) BLDC operation mode. (b) BLAC operation mode.

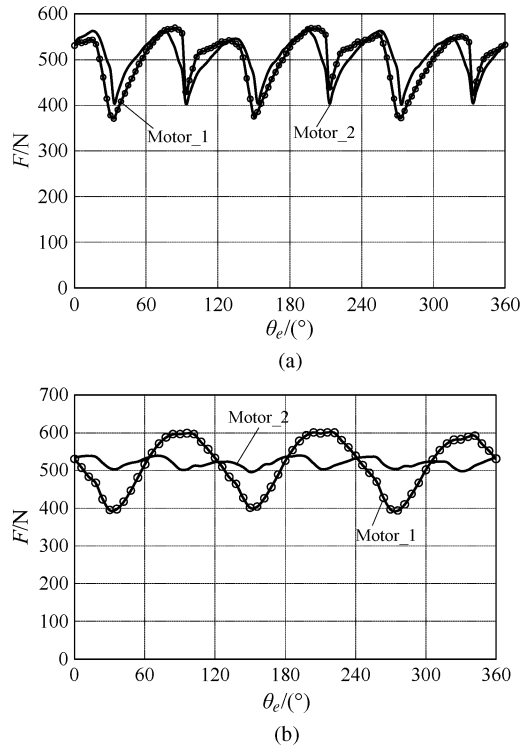

Fig. 19. The electromagnetic thrust force of both motors under BLDC and BLAC operation modes. (a) BLDC operation mode. (b) BLAC operation mode.

offer higher thrust force and much lower force ripple especially under BLAC operation than Motor_1.

TABLE III
ELECTROMAGNETIC THRUST FORCE CAPABILITY COMPARISON

	BLDC		BLAC	
	Motor_1	Motor_2	Motor_1	Motor_2
F_{e_max} (N)	569.6	567.6	601.3	540.1
F_{e_min} (N)	370.9	403.1	393.6	495.2
F_{e_rip} (N)	198.7	164.5	207.7	44.9
F_{e_avg} (N)	501	506.1	514.7	520

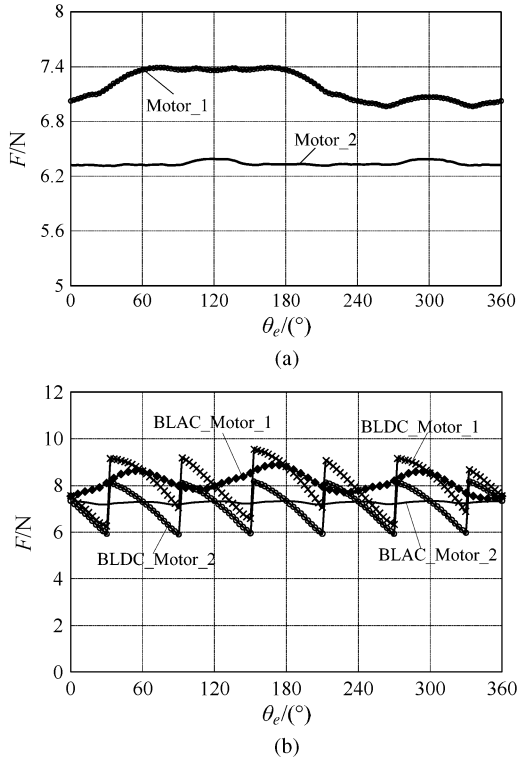

Fig. 20. Normal force of both motors. (a) No-load. (b) Load.

TABLE IV
NORMAL FORCE CAPABILITY COMPARISON

	Motor_1 (kN)			Motor_2 (kN)		
	No-load	BLDC	BLAC	No-load	BLDC	BLAC
F_{N_max}	7.389	9.161	8.895	6.389	8.169	7.348
F_{N_min}	6.963	6.343	7.452	6.31	5.925	7.194
F_{N_rip}	0.426	2.818	1.443	0.079	2.244	0.154
F_{N_avg}	7.188	8.024	8.152	6.337	7.184	7.284

Fig. 20 shows the normal force of both motors at different load conditions. The detailed results are listed in Table IV. It can be seen that the ripple of normal force of Motor_2 at no-load and BLAC load conditions are about 18.5% and 10.7% of that of Motor_1, respectively.

IV. CONCLUSION

In this paper, a modular and complementary LDSPM motor has been proposed for long stator applications. This motor possesses a simple iron stator which offers the advantage of low cost and robustness over conventional PMLM. Also, compared with the existing LDSPM motor, the proposed LDSPM motor

can greatly reduce mover weight, mover length, and the magnet usage. Moreover, the modular mover structure is very convenient to manufacture. By using FEM, the validity of the proposed LDSPM motor has been verified. The results confirm that the proposed LDSPM motor can offer symmetrical back-EMF, lower inductance variation range with mover position, bigger average thrust force as well as greatly reduced cogging force and reluctance force ripple especially under BLAC operation. However, the proposed motor also possesses two drawbacks which need to be addressed, which are the high mover and higher stator flux density than those of Motor_1.

ACKNOWLEDGMENT

This work was supported in part by the National Natural Science Foundation of China (Project No: 50907031), the Specialized Research Fund for the Doctoral Program of Higher Education of China (Project No: 20090092110034), and the 2010 foundation project of technology innovation for graduate in Jiangsu Province (X10B_066Z).

REFERENCES

[1] Y. Liao, F. Liang, and T. A. Lipo, "A novel permanent magnet machine with doubly salient structure," in *Proc. IEEE IAS Annu. Conf.*, 1992, pp. 308–314.

[2] R. P. Deodhar, S. Andersson, I. Boldea, and T. J. E. Miller, "The flux-reversal machine: A new brushless doubly-salient permanent-magnet machine," in *Proc. IEEE IAS Annu. Conf.*, 1996, pp. 786–793.

[3] E. Hoang, A. H. Ben-Ahmed, and J. Lucidarme, "Switching flux permanent magnet polyphased machines," in *Proc. Eur. Conf. Power Electron. Appl.*, 1997, pp. 903–908.

[4] M. Cheng, K. T. Chau, and C. C. Chan, "New split-winding doubly salient permanent magnet motor drive," *IEEE Trans. Aerosp. Electron. Syst.*, vol. 39, no. 1, pp. 202–210, Jan. 2003.

[5] K. T. Chau, Q. Sun, Y. Fan, and M. Cheng, "Torque ripple minimization of doubly salient permanent-magnet motors," *IEEE Trans. Energy Convers.*, vol. 20, no. 2, pp. 352–358, Jun. 2005.

[6] T. H. Kim, S. H. Won, and K. Bong *et al.*, "Reduction of cogging torque in flux-reversal machine by rotor teeth pairing," *IEEE Trans. Magn.*, vol. 41, no. 10, pp. 3964–3966, Oct. 2005.

[7] T. H. Kim, K. B. Jang, and Y. D. Chun *et al.*, "Comparison of the characteristics of a flux reversal machine under the different driving methods," *IEEE Trans. Magn.*, vol. 41, no. 5, pp. 1916–1919, May 2005.

[8] Z. Q. Zhu and J. T. Chen, "Advanced flux-switching permanent magnet brushless machines," *IEEE Trans. Magn.*, vol. 46, no. 6, pp. 1447–1453, Jun. 2010.

[9] W. Hua, M. Cheng, and Z. Q. Zhu *et al.*, "Analysis and optimization of back EMF waveform of a flux-switching permanent magnet motor," *IEEE Trans. Energy Convers.*, vol. 23, no. 3, pp. 727–733, Sep. 2008.

[10] M. Cheng, W. Hua, J. Zhang, and W. Zhao, "Overview of stator-permanent magnet brushless machines," *IEEE Trans. Ind. Electron.*, in press.

[11] R. Cao, M. Cheng, W. Hua, W. Zhao, and Y. Du, "A new primary permanent magnet linear motor for urban rail transit," in *Proc. ICEMS2010*, Incheon, Korea, Oct. 2010, pp. 1528–1532.

[12] C. E. Lampson, "Polyphase Sawyer Motor Forcer," U.S. Patent US 7148590 B1, Dec. 12, 2006.

[13] S.-U. Chung, D.-H. Kang, J.-H. Chang, J.-W. Kim, and J.-Y. Lee, "New configuration of flux reversal linear synchronous motor," in *Proc. ICEMS2007*, Seoul, Korea, Oct. 2007, pp. 864–867.

[14] S.-U. Chung, H.-J. Lee, and S.-M. Hwang, "A novel design of linear synchronous motor using FRM topology," *IEEE Trans. Magn.*, vol. 44, no. 6, pp. 1514–1517, Jun. 2008.

[15] P. Smit, "Forcer and Associated Three Phase Linear Motor System," U.S. Patent US 6798089 B1, Sep. 28, 2004.

[16] H. Lin and J. A. Heilig, "Linear Hybrid Brushless Servo Motor," U.S. Patent US 7230355 B2, Jun. 12, 2007.

[17] Z. Q. Zhu, X. Chen, and J. Chen, "Novel linear flux switching permanent magnet machines," in *Proc. ICEMS2008*, Wuhan, China, Oct. 2008, pp. 2948–2953.

[18] M. Jin, C. Wang, and J. Shen, "A modular permanent magnet flux-switching linear machine with fault tolerant capability," *IEEE Trans. Magn.*, vol. 45, no. 8, pp. 3179–3186, Aug. 2009.

[19] S. W. Youn, J. J. Lee, H. S. Yoon, and C. S. Koh, "A new cogging-free permanent-magnet linear motor," *IEEE Trans. Magn.*, vol. 44, no. 7, pp. 1785–1790, Jul. 2008.

[20] S. Chung, H. Lee, and B. Woo *et al.*, "A feasibility study on a new doubly salient permanent magnet linear synchronous machine," *IEEE Trans. Magn.*, vol. 46, no. 6, pp. 1572–1575, Jun. 2010.

[21] B. Kou, H. Wu, and L. Li *et al.*, "The thrust characteristics investigation of double-side plate permanent magnet linear synchronous motor for EML," *IEEE Trans. Magn.*, vol. 45, no. 1, pp. 501–505, Jan. 2009.

[22] N. Bianchi, S. Bolognani, and A. D. F. Cappello, "Reduction of cogging force in PM linear motors by pole-shifting," *IEE Proc. Elect. Power Appl.*, vol. 152, no. 3, pp. 703–709, May 2005.

[23] W. Zhao, K. T. Chau, M. Cheng, J. Ji, and X. Zhu, "Remedial brushless AC operation of fault-tolerant doubly salient permanent-magnet motor drives," *IEEE Trans. Ind. Electron.*, vol. 57, no. 6, pp. 2134–2141, Jun. 2010.

[24] Y. Gong, K. T. Chau, J. Z. Jiang, C. Yu, and W. Li, "Design of doubly salient permanent magnet motors with minimum torque ripple," *IEEE Trans. Magn.*, vol. 45, no. 10, pp. 4704–4707, Oct. 2009.

[25] C.-F. Wang, J.-X. Shen, and Y. Wang, "A new method for reduction of detent force in permanent magnet flux-switching linear motors," *IEEE Trans. Magn.*, vol. 45, no. 6, pp. 2843–2846, Jun. 2009.

[26] H. S. Lim, R. Krishnan, and N. S. Lobo, "Design and control of a linear propulsion system for an elevator using linear switched reluctance motor drives," *IEEE Trans. Ind. Electron.*, vol. 55, no. 2, pp. 534–542, Feb. 2008.

[27] M. Cheng, K. T. Chau, and C. C. Chan, "Design and analysis of a new doubly salient permanent magnet motor," *IEEE Trans. Magn.*, vol. 37, no. 4, pp. 3012–3020, Jul. 2001.

[28] X. Zhu, M. Cheng, W. Hua, J. Zhang, and W. Zhao, "Design and analysis of a new hybrid excited doubly salient machine capable of field control," in *IEEE 41st IAS Annu. Meeting Record*, Oct. 2006, pp. 2382–2389.

[29] W. Zhao, M. Cheng, W. Hua, H. Jia, and R. Cao, "Back-EMF harmonic analysis and fault-tolerant control of flux-switching permanent-magnet machine with redundancy," *IEEE Trans. Ind. Electron.*, vol. 58, no. 5, pp. 1926–1935, May 2011.

[30] W. Zhao, M. Cheng, X. Y. Zhu, W. Hua, and X. Kong, "Analysis of fault-tolerant performance of a doubly salient permanent-magnet motor drive using transient co-simulation method," *IEEE Trans. Ind. Electron.*, vol. 55, no. 4, pp. 1739–1748, Apr. 2008.

[31] J. Faiz, M. Ebrahimi-Salari, and G. Shahgholian, "Reduction of cogging force in linear permanent-magnet generators," *IEEE Trans. Magn.*, vol. 46, no. 1, pp. 135–140, Jan. 2010.

[32] M. A. Shabani, J. Milimonfared, and S. Taghipour, "Cogging force mitigation of tubular permanent magnet machines with magnet dividing," in *Proc. ICEMS2007*, Soul, Korea, Oct. 2007, pp. 810–814.

[33] Z. Q. Zhu, Y. Pang, D. Howe, S. Iwasaki, R. Deodhar, and A. Pride, "Analysis of electromagnetic performance of flux-switching permanent-magnet machines by nonlinear adaptive lumped parameter magnetic circuit model," *IEEE Trans. Magn.*, vol. 41, no. 11, pp. 4277–4287, Nov. 2005.

[34] M. Cheng, K. T. Chau, and C. C. Chan, "Static characteristics of a new doubly salient permanent magnet motor," *IEEE Trans. Energy Convers.*, vol. 16, no. 1, pp. 20–25, Mar. 2001.

[35] Z. Q. Zhu, J. X. Shen, and D. Howe, "Flux-weakening characteristics of trapezoidal back-emf machines in brushless DC and AC modes," in *Proc. CES/IEEE Int. Power Electron. Motion Control Conf.*, Shanghai, China, 2006, pp. 908–912.

Ruiwu Cao (S'10) was born in Jiangsu, China, in 1980. He received the B.S. degree from Yancheng Institute of Technology, Yancheng, China, in 2004, and the M.S. degree from Southeast University, Nanjing, China, in 2007. He is currently working toward the Ph.D. degree at Southeast University, Nanjing, China, all in electrical engineering.

He joined Bosch and Siemens Household (BSH) Electrical Appliances, Nanjing, Jiangsu, China, as a Hardware Electrical Engineer from 2007 to 2009. From 2010, he was a joint Ph.D. student founded by China Scholarship Council with the College of Electrical and Computer Science, University of Michigan, Dearborn, where he worked on permanent magnet motors. His areas of interests include design, analysis, and control of permanent-magnet linear machines.

Ming Cheng (M'01–SM'02) received the B.S. and M.S. degrees from the Department of Electrical Engineering, Southeast University, China, in 1982 and 1987, respectively, and Ph.D. degree from the Department of Electrical and Electronic Engineering, The University of Hong Kong, Hong Kong, in 2001.

Since 1987, he has been with Southeast University, where he is currently a Professor in the School of Electrical Engineering and the Director of the Research Center for Wind Power Generation. His teaching and research interests include electrical machines, motor drives for electric vehicles and renewable energy generation. He has authored or coauthored over 250 technical papers and 4 book, and holds 50 patents in these areas.

Prof. Cheng is a Fellow of IET. He has served as chair and organizing committee member for many international conferences.

Chris Mi (S'00–A'01–M'01–SM'03) received the B.S. and M.S. degrees from Northwestern Polytechnical University, Xi'an, China, and the Ph.D. degree from the University of Toronto, Toronto, ON, Canada, all in electrical engineering.

He is an Associate Professor with the University of Michigan, Dearborn. He was with General Electric Company from 2000 to 2001.

Prof. Mi is a recipient of the National Innovation Award, the Government Special Allowance, and the 2005 Distinguished Teaching Award from the University of Michigan. He is also the recipient of the 2007 IEEE Region 4 Outstanding Engineer Award, the 2007 IEEE Southeastern Michigan Section Outstanding Professional Award, and the 2007 SAE E2T Award.

Wei Hua (M'07) was born in Jiangsu, China, in 1978. He received the B.S. and Ph.D. degrees in 2001 and 2007, respectively, from Southeast University, Nanjing, China, both in electrical engineering.

He is currently with Southeast University, where he is an Associate Professor and Deputy Dean of Electrical Machines and Control Department. His areas of interests include design, analysis and control of the novel permanent magnet machines. He has authored more than 60 published papers on these topics.

Wenxiang Zhao (M'08) was born in Jilin, China, in 1976. He received the B.S. and M.S. degrees in electrical engineering from Jiangsu University, Zhenjiang, China, in 1999 and 2003, respectively, and the Ph.D. degree in electrical engineering at Southeast University, Nanjing, China, in 2010.

Since 2003, he has been with Jiangsu University, where he is currently an Associate Professor in the School of Electrical Information Engineering. His areas of interests include electric machine design, modeling, fault analysis, and intelligent control.